Probing temperature during laser spot welding from vapor composition and modeling

X. He and T. DebRoy[a)]
Department of Materials Science and Engineering, The Pennsylvania State University, University Park, Pennsylvania 16802-5005

P. W. Fuerschbach
Joining and Coating Department, Sandia National Laboratories, Albuquerque, New Mexico 87185

(Received 16 June 2003; accepted 4 September 2003)

Measurement of weld pool temperature during laser spot welding is a difficult task because of the short pulse duration, often lasting only a few milliseconds, highly transient nature of the process, and the presence of a metal vapor plume near the weld pool. This article describes recent research to estimate weld pool temperatures experimentally and theoretically. Composition of the metal vapor from the weld pool was determined by condensing a portion of the vapor on the inner surface of an open ended quartz tube which was mounted perpendicular to the sample surface and coaxial with the laser beam. It was found that iron, chromium, and manganese were the main metallic species in the vapor phase. The concentrations of Fe and Cr in the vapor increased slightly while the concentration of Mn in the vapor decreased somewhat with the increase in power density. The vapor composition was used to determine an effective temperature of the weld pool. A transient, three-dimensional numerical heat transfer and fluid flow model based on the solution of the equations of conservation of mass, momentum and energy was used to calculate the temperature and velocity fields in the weld pool as a function of time. The experimentally determined geometry of the spot welds agreed well with that determined from the computed temperature field. The effective temperature determined from the vapor composition was found to be close to the numerically computed peak temperature at the weld pool surface. Because of the short process duration and other serious problems in the direct measurement of temperature during laser spot welding, estimating approximate values of peak temperature from metal vapor composition is particularly valuable. [DOI: 10.1063/1.1622118]

I. INTRODUCTION

Laser spot welding is characterized by highly transient nature and very short duration of the process. The welding is often completed in a few milliseconds and the heating and cooling rates attained are many times higher than those typical in steady-state linear laser welding process.[1] Knowledge of temperature and velocity fields, solidification rate, and thermal cycles are important to determine the geometry, composition, structure, and the resulting properties of the spot welds.[1,2] Understanding the formation of nonequilibrium phases and solidification cracking based on fundamental principles requires knowledge of the heating and cooling rates. Experimental measurements of temperature and velocity fields during laser spot welding are difficult because of the insufficient time for measurement and the highly transient nature of the welding process. In addition, the weld pool is often covered by a metal vapor plume. Because of these difficulties, no generally available technique has been developed to date to measure temperature and velocity fields in the weld pool during laser spot welding.

During high energy laser beam welding of important engineering alloys, the metal in the weld pool can be heated to very high temperatures and significant vaporization of volatile alloying elements often takes place from the weld pool surface.[3–12] The loss of alloying elements can result in significant changes in the microstructure and degradation of mechanical properties of weldments. During welding of stainless steels, the main constituents of the metal vapor are iron, manganese, chromium, and nickel.[9,11–13] In high manganese stainless steels, such as AISI 201, iron and manganese are the prominent vapor species in the welding environment. In order to minimize the mass loss during high power laser welding, it is necessary to quantitatively understand the role of various factors that affect the alloying element vaporization. The most important factors in determining the rate of vaporization of different elements are the temperature distribution on the surface and the weld metal chemical composition.

During laser welding, a strong spatial gradient of temperature exists on the weld pool surface. The resulting gradient of surface tension is the main driving force for the strong recirculating flow of molten metal in the weld pool.[14–16] In addition, the buoyancy force resulting from the spatial variation of density also contributes to the motion of the weld pool, although to a much lesser extent than the surface tension gradient. Because of the strong recirculating flow, the weld pool can be reasonably assumed to be well

[a)]Author to whom correspondence should be addressed; electronic mail: debroy@psu.edu

mixed and compositionally homogeneous. For a weld pool of known composition, the vaporization rates of various alloying elements are strongly affected by the surface temperatures. Since the middle region of the weld pool surface is at a much higher temperature than the periphery, it is fair to expect that much of the vaporized species originate from the middle of the weld pool surface. Since the relative rates of vaporization of two alloying elements are determined by the local temperature, the measured vapor composition can provide a rough idea of the peak temperature at the weld pool surface.

In recent decades, numerical models have been developed to understand the heat transfer and fluid flow during welding. These models have been widely utilized to quantitatively understand thermal cycles and fusion zone geometry.[17–25] Results from the heat transfer and fluid flow study have also been used to study weld metal phase composition,[26–28] inclusion structure,[29–31] grain structure,[32–34] and for prevention of porosity in welds.[35] However, most of these studies were focused on linear steady state welds and not on very short duration laser spot welds. Although a limited number of investigations of spot welds have been undertaken in the past, the time scales studied were much longer than the typical few milliseconds involved in laser spot welds. A detailed experimental and theoretical study of laser spot welding has not been undertaken.

In this article, recent theoretical and experimental research to estimate weld pool temperatures are described. A transient, three-dimensional numerical heat transfer and fluid flow model based on the solution of the equations of conservation of mass, momentum and energy was used to calculate the temperature and velocity fields in the weld pool as a function of time. The effects of spatial variation of surface tension and buoyancy were considered to determine the weld pool convection as a function of time. Very fine grids and small time steps were used to achieve accuracy in the calculations. The model was tested by comparing the experimentally determined geometry of the spot welds with those obtained from the computed temperature fields. Composition of the metal vapor from the weld pool was determined by condensing a portion of the vapor on the inner surface of a both end open quartz tube which was mounted perpendicular to the sample surface and co-axial with the laser beam. The vapor composition was used to determine an effective temperature of the weld pool for various welding conditions. This technique is shown to be a useful method to determine rough values of peak temperature during laser spot welding. No other reliable method for the estimation of peak temperature during laser spot welding has emerged so far because of the very short duration and highly transient nature of the laser spot welding process.

II. EXPERIMENTAL PROCEDURE

Several 304 stainless steel laser spot welds were fabricated at the Sandia National Laboratories. The alloy composition was: 1 wt % Mn, 18.1 wt % Cr, 8.6 wt % Ni, 0.69 wt % Si, 0.046 wt % C, 0.012 wt % P, 0.003 wt % S, and balance Fe. A schematic diagram of the experimental setup is presented in Fig. 1. During laser spot welding, a cylindrical 6 mm inner diameter by 25 mm long, open ended quartz tube was placed coaxial to the laser beam and right above the 304 stainless steel samples. The vaporized elements were collected as condensation on the interior surface of the tube. A Raytheon SS 525 pulsed Nd:YAG laser was used for laser spot welding with pulse energies of 2.12 and 3.19 J and pulse durations of 4.0 and 3.0 ms, respectively. The laser beam was focused inside the quartz tube with a 100 mm focal length lens. For each combination of energy and duration, the laser beam was defocused to different extents to obtain various spot diameters and power densities. To increase the amount of vapor condensate collected, 50 individual spot welds were made on each of the 3 by 10 by 17 mm samples.. The spot welds were made in ambient air since it was impractical to provide inert gas shielding inside the quartz tube for each spot weld. The experimental parameters are indicated in Table I.

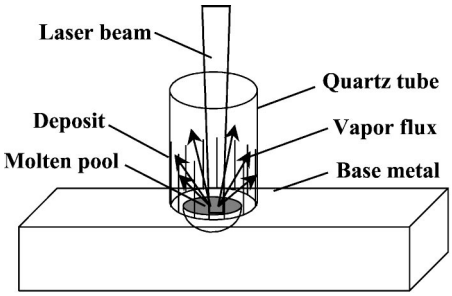

FIG. 1. A schematic diagram of the experimental setup.

The quatz tube samples were examined using the JEOL 8600 Electron Microprobe x-ray analyzer to determine the vapor composition. The evaporation products had the consistency of fine dust. The quartz tubes were broken and a suitable fragment from each experiment was mounted to expose the deposit. Due to the geometry of the samples and their highly porous nature, the probe was not operated in an automated mode. Instead a series of spot measurements of the K values (count rate ratios of unknown to standards) were made on each sample. The K value measurements were converted to approximate oxide ratios and averaged together for each sample.

III. MATHEMATICAL FORMULATION

A. Assumptions

The weld metal was assumed to be incompressible, Newtonian fluid. Constant thermophysical properties were

TABLE I. Welding parameters.

Sample No.	Pulse energy (J)	Beam radius (mm)	Power density (W/mm^2)	Pulse duration (ms)
E	2.12	0.289	2020	4
B/F	2.12	0.247	2765	4
C	2.12	0.227	3274	4
D	2.12	0.171	5769	4
G	3.19	0.326	3185	3
A	3.19	0.28	4317	3

used for the calculations and the variation of absorption coefficient of the laser by the stainless steel at different temperatures was ignored for simplicity.

B. Governing equations

Because of the axisymmetric nature of the spot welding, the governing equations can be solved in two dimensions to calculate the temperature and velocity fields. However, since the model is also used for welding with a moving heat source, a transient, three-dimensional, heat transfer and fluid flow model was used for the laser spot welding. The following momentum conservation equation was solved:[36]

$$\rho\frac{\partial u_j}{\partial t}+\rho\frac{\partial(u_i u_j)}{\partial x_i}=\frac{\partial}{\partial x_i}\left(\mu\frac{\partial u_j}{\partial x_i}\right)+S_j, \tag{1}$$

where ρ is the density, t is the time, x_i is the distance along the $i=1$, 2, and 3 directions, u_j is the velocity component along the j direction, μ is the effective viscosity, and S_j is the source term for the jth momentum equation and is given as

$$S_j=-\frac{\partial p}{\partial x_j}+\frac{\partial}{\partial x_j}\left(\mu\frac{\partial u_j}{\partial x_j}\right)-C\left(\frac{(1-f_L)^2}{f_L^3+B}\right)u_j+\rho g\beta(T-T_{\mathrm{ref}}), \tag{2}$$

where p is the pressure, f_L is the liquid fraction, B is a constant introduced to avoid division by zero, C ($=1.6\times10^4$) is a constant that takes into account mushy zone morphology, β is the coefficient of volume expansion, and T_{ref} is a reference temperature. The third term on the right hand side (RHS) represents the frictional dissipation in the mushy zone according to the Carman–Kozeny equation for flow through a porous media.[37,38] The value of the effective viscosity in Eq. (1) is a property of the specific welding system and not an inherent property of the liquid metal. Typical values of effective viscosity are much higher than that of the molecular viscosity.[24,25] The higher value is important, since it allows accurate modeling of the high rates of transport of momentum in systems with strong fluctuating velocities that are inevitable in small weld pools with very strong convection currents. The pressure field was obtained by solving the following continuity equation simultaneously with the momentum equation:

$$\frac{\partial(\rho u_i)}{\partial x_i}=0. \tag{3}$$

The total enthalpy H is represented by a sum of sensible heat h and latent heat content ΔH, i.e., $H=h+\Delta H$, where $h=\int C_p dT$, C_p is the specific heat, T is the temperature, $\Delta H=f_L L$, L is the latent heat of fusion, and the liquid fraction f_L is assumed to vary linearly with temperature in the mushy zone

$$f_L=\begin{cases}1 & T>T_L\\ \dfrac{T-T_S}{T_L-T_S} & T_S\leqslant T\leqslant T_L\\ 0 & T<T_S\end{cases}, \tag{4}$$

where T_L and T_S are the liquidus and solidus temperature, respectively. The thermal energy transport in the weld workpiece can be expressed by the following modified energy equation:[2,23]

$$\rho\frac{\partial h}{\partial t}+\rho\frac{\partial(u_i h)}{\partial x_i}=\frac{\partial}{\partial x_i}\left(\frac{k}{C_p}\frac{\partial h}{\partial x_i}\right)-\rho\frac{\partial(\Delta H)}{\partial t}-\rho\frac{\partial(u_i\Delta H)}{\partial x_i}, \tag{5}$$

where k is the thermal conductivity. In the liquid region, the value of the thermal conductivity in Eq. (5) is taken as the effective thermal conductivity which is a property of the specific welding system and not an inherent property of the liquid metal. Typical values of effective thermal conductivity are much higher than that of the thermal conductivity of the liquid. The higher value is important, since it allows accurate modeling of the high rates of transport of heat in systems with strong fluctuating velocities that are inevitable in small weld pools with very strong convection currents.[24,25] The weld top surface is assumed to be flat. The velocity boundary condition is given as[2]

$$\mu\frac{\partial u}{\partial z}=f_L\frac{d\gamma}{dT}\frac{\partial T}{\partial x},\qquad \mu\frac{\partial v}{\partial z}=f_L\frac{d\gamma}{dT}\frac{\partial T}{\partial y},\qquad w=0, \tag{6}$$

where u, v, and w are the velocity components along the x, y, and z directions, respectively, and $d\gamma/dT$ is the temperature coefficient of surface tension. As shown in this equation, the u and v velocities are determined from the Marangoni effect. The w velocity is equal to zero since there is no flow of liquid metal perpendicular to the pool top surface. The heat flux at the top surface is given as

$$k\frac{\partial T}{\partial z}=\frac{fQ\eta}{\pi r_b^2}\exp\left(-\frac{f(x^2+y^2)}{r_b^2}\right)-\sigma\varepsilon(T^4-T_a^4)-h_c(T-T_a), \tag{7}$$

where f is the power density distribution factor, Q is the total energy of the heat source, η is the absorption coefficient, r_b is the heat source radius, σ is the Stefan–Boltzmann constant, h_c is the heat transfer coefficient, and T_a is the ambient temperature. The first term on the RHS is the heat input from the heat source. The second and third terms represent the heat loss by radiation and convection, respectively. For laser welding, laser power density distribution factor f is taken as[39] 3.0. Laser power and beam radius were experimentally measured. The reported values of the absorption coefficient vary significantly.[40–42] For example, Cremers *et al.*[40] indicated absorption coefficient of Nd:YAG laser in 316 stainless steel in the range of 0.21–0.62. The absorption coefficient has been related to the substrate resistivity and the wavelength of the laser radiation by the following relation:[42]

$$\eta(T)=0.365\left(\frac{\alpha}{\lambda}\right)^{1/2}-0.0667\left(\frac{\alpha}{\lambda}\right)+0.006\left(\frac{\alpha}{\lambda}\right)^{3/2}, \tag{8}$$

TABLE II. Data used for calculations.

Property/Parameter	Value[a]
Density of liquid metal (kg/m^3)	7.2×10^3
Absorption coefficient	0.27
Effective viscosity (kg/m s)	0.1
Solidus temperature (K)	1697
Liquidus temperature (K)	1727
Enthalpy of solid at melting point (J/kg)	1.20×10^6
Enthalpy of liquid at melting point (J/kg)	1.26×10^6
Specific heat of solid (J/kg K)	711.8
Specific heat of liquid (J/kg K)	837.4
Thermal conductivity of solid (J/m s K)	19.26
Effective thermal conductivity of liquid (J/m s K)	209.3
Temperature coefficient of surface tension (N/m K)	-0.43×10^{-3}
Coefficient of thermal expansion	1.96×10^{-5}

[a]See Refs. 43–47.

where λ is the wavelength (cm) and α is the electrical resistivity of the materials (Ω cm). The average electrical resistivity of 304 stainless steel is 80 $\mu\Omega$ cm,[43] and the wavelength of Nd:YAG laser is 1.064 μm. Substituting these values into Eq. (8), the absorption coefficient is obtained as 0.27, which is the value taken in the calculations reported in this article. The data used for calculations[43–47] are presented in Table II. The boundary conditions are defined as zero flux across the symmetric surface as

$$\frac{\partial u}{\partial y}=0,\ v=0,\ \frac{\partial w}{\partial y}=0, \tag{9}$$

$$\frac{\partial h}{\partial y}=0. \tag{10}$$

At all other surfaces, temperatures are set at ambient temperature and the velocities are set to be zero.

The governing equations were discretized and solved iteratively on a line-by-line basis using a tridiagonal matrix algorithm. The detailed procedure to solve the equations is described in the literature.[36] After obtaining the values of the sensible enthalpy, h, on computational domain, temperature can be expressed as

$$T=\begin{cases} T_{\text{solid}}+\dfrac{h-H_{\text{melt}}}{C_{\text{ps}}} & \text{for } h\leqslant H_{\text{melt}} \\ T_{\text{solid}}+\dfrac{h-H_{\text{melt}}}{C_{\text{pa}}}=T_{\text{solid}}+\dfrac{h-H_{\text{melt}}}{H_{\text{cal}}-H_{\text{melt}}}(T_{\text{liquid}}-T_{\text{solid}}) & \\ \quad =T_{\text{solid}}+f_l\times(T_{\text{liquid}}-T_{\text{solid}}) & \text{for } H_{\text{melt}}<h<H_{\text{cal}} \\ T_{\text{liquid}}+\dfrac{h-H_{\text{cal}}}{C_{\text{pl}}} & \text{for } h\geqslant H_{\text{cal}} \end{cases}, \tag{11}$$

where T_{solid} and T_{liquid} are the solidus and liquidus temperatures of the material, respectively. H_{melt} is the total enthalpies at the liquidus temperatures, C_{ps} and C_{pl} are the specific heat of solid and liquid, respectively, and f_l is the liquid fraction. The specific heat, C_{pa}, in the mushy zone was calculated by

$$C_{\text{pa}}=(C_{\text{ps}}+C_{\text{pl}})/2. \tag{12}$$

H_{cal} is given as

$$H_{\text{cal}}=H_{\text{melt}}+C_{\text{pa}}\times(T_{\text{liquid}}-T_{\text{solid}}). \tag{13}$$

IV. RESULTS AND DISCUSSION

The local evaporation flux of an alloying element based on the Langmuir equation is expressed as[48]

$$J_i=\frac{\lambda P_i}{\sqrt{2\pi M_i R T}}, \tag{14}$$

where J_i is the vaporization flux of the element i, λ is positive constant with a maximum value of 1 that accounts for the inevitable condensation of a portion of the vaporized atoms on the surface at pressures higher than perfect vacuum, P_i is the vapor pressure of i over the liquid, M_i is molecular weight of the vaporizing element i, R is the gas constant, and T is the temperature. At pressures close to atmospheric pressure, the value of λ cannot be estimated from fundamental principles. The lack of knowledge of λ poses a problem in the application of Langmuir equation for quantitative calculation of the vaporization rates of individual alloying elements. However, since the relative vaporization rates of any two alloying elements is independent of λ, Langmuir equation can be used for predicting the relative vaporization rates of various alloying elements:

$$\frac{J_i}{J_j}=\frac{P_i}{P_j}\left(\frac{M_j}{M_i}\right)^{1/2}. \tag{15}$$

The equilibrium partial pressure P_i over the alloy depends upon the composition and the temperature of the weld metal. The vapor pressures of the alloying elements over pure liquids are presented in Fig. 2(a) and those over 304 stainless steel are shown in Fig. 2(b). The equilibrium vapor pressure data used in the calculations are presented in the Appendix. It can be seen from Fig. 2(a) that among the four alloying elements, manganese has the highest vapor pressure over its pure liquid in the entire temperature range studied. However, its vapor pressure over the alloy is lower than those of iron and chromium, as observed from Fig. 2(b). This is because manganese only accounts for 1.0 wt % in 304 stainless steel while iron and chromium are present at 72.3 and 18.1 wt %, respectively. It can be seen from Fig. 2(b) that over liquid stainless steel, iron is the dominant vaporizing species, followed by chromium and manganese. The vapor pressure of nickel over the alloy is very low. Vapor pressures of all the alloying elements are strong functions of temperature.

The extent of variation of the equilibrium partial pressures resulting from temperature change is different for different elements. Since the vaporization flux of the individual elements are proportional to their equilibrium partial pressures, the ratio of the vaporization flux of any two elements can be a strong function of temperature. Consequently, if the vapor composition, i.e., the ratio of the vaporization flux of any two elements is known, the weld pool temperature can be determined. The experimentally determined concentrations of iron, chromium and manganese in the vapor condensate as a function of laser power density are shown in Figs.

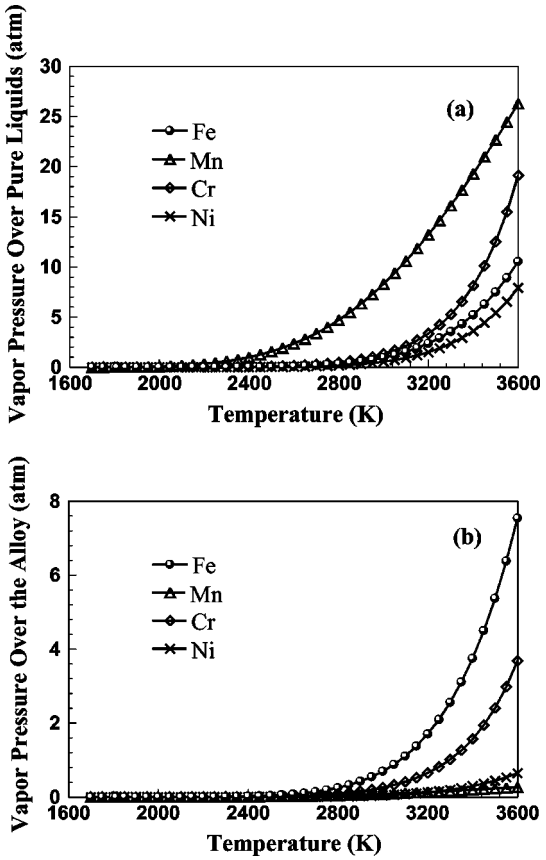

FIG. 2. Equilibrium vapor pressures of the four alloying elements (a) over respective pure liquids and (b) over the alloy at different temperatures.

3(a), 3(b), and 3(c), respectively. Figure 3(a) shows that as the power density increases, the concentration of Fe in the vapor condensate increases. This is because of the slope of the vapor pressure versus temperature plot for iron is steeper than those of the other alloying elements as shown in Fig. 2(b). For similar reason, the concentration of chromium in the vapor condensate increases slightly with power density. On the other hand, the concentration of manganese decreases with power density. Again, the reason for this behavior can be traced to the manner in which the equilibrium vapor pressure of manganese varies with temperature relative to other alloying elements.

Using the vapor pressures of various alloying elements over liquid stainless steel presented in Fig. 2(b), the values of J_{Fe}/J_{Mn} and J_{Cr}/J_{Mn} are calculated from Eq. (15) as a function of temperature. The computed values are shown in Fig. 4. It is observed that both the ratios of the vaporization fluxes depend strongly on temperature. So, if the vapor composition is known, an effective temperature of the weld pool can be determined. Using the experimentally determined vapor composition data presented in Figs. 3(a), 3(b), and 3(c) and the J_{Fe}/J_{Mn} and J_{Cr}/J_{Mn} versus temperature plots in Fig. 4, effective weld pool temperatures can be determined for various power densities. The results are shown in Fig. 5. It can be observed that the temperatures calculated from J_{Fe}/J_{Mn} are in good agreement with those obtained from J_{Cr}/J_{Mn}, indicating that the estimated effective temperatures are independent of the choice of element pairs.

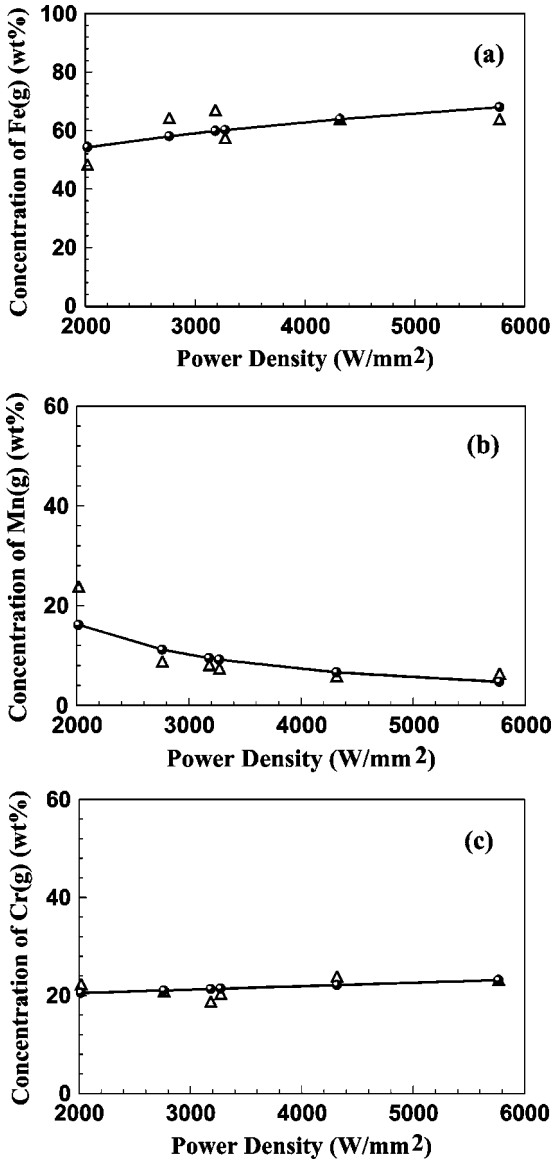

FIG. 3. Measured weight percent of (a) Fe, (b) Mn, and (c) Cr in vapor composition with laser power density. The triangles represent the original data and the circles show best fit.

What does the effective temperature mean? Let us consider a relatively simple isothermal system where the vaporization of alloying elements occurs from the surface of a stainless steel melt. The relative vaporization rates as a function of temperature would be given by Fig. 4. Since the vapor composition at the effective vaporization temperature is the same as that obtained from the welding experiment, the effective temperature can be defined as a temperature that results in the same vapor composition as the welding experiment. During welding, the vapors originate from the entire weld pool surface where there is a strong variation of temperature. Since the vaporization rate increases strongly with temperature, most of the vapors originate from the middle of the weld pool. Furthermore, the temperature profile changes with time. It will be shown later in this article that for the conditions of the experiments described the surface temperature change is most pronounced in the first millisecond. The changes in temperature slows down considerably after that

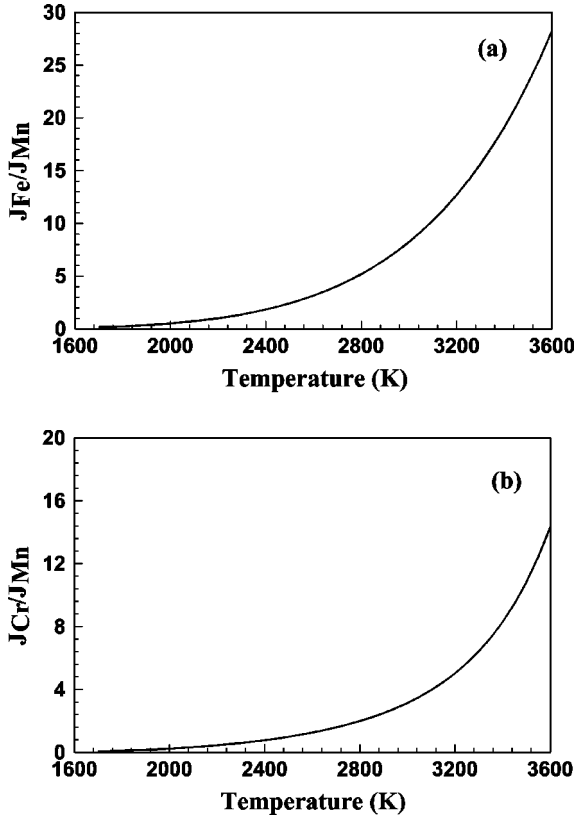

FIG. 4. The ratio of calculated vaporization rates of (a) Fe and Mn and (b) Cr and Mn as a function of temperature

time. As a result most of the vapor comes from the later portion of the thermal cycle when the temperature is fairly close to the value at the end of the pulse. In short, since much of the vapor originates from the middle of the weld pool surface and towards the end of the pulse, the effective temperature is expected to be fairly close to the peak temperature.

The experimentally determined weld pool cross sections are compared with the corresponding numerically computed values in Fig. 6. It is observed that the calculated weld pool geometry and dimensions agree well with the experimental results. The good agreement indicates the validity of the transient heat transfer and fluid flow model. The experimental and calculated values of weld pool depth and width for various laser power densities are presented in Fig. 7. The total power was kept constant at 1967 W while the beam radius was varied to obtain different power densities. It can be seen that the calculated weld pool depth and width show good agreement with the experimental results at low power densities. However, at high power densities, there is some difference between the calculated and the experimental values of the weld pool depth. In order to understand the reason for the discrepancy, the experimental ratio of weld pool depth to half-width is presented in Fig. 8. It is observed that the ratio varied between 0.4 and 0.7 at power densities below

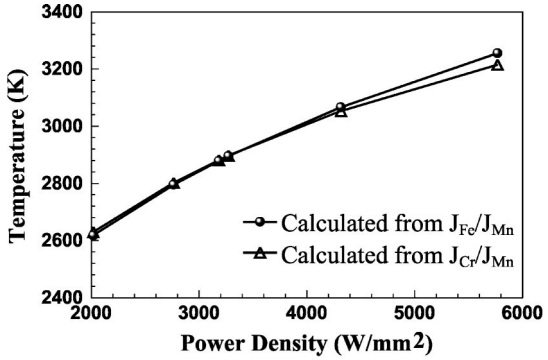

FIG. 5. Temperature values calculated from the ratio of vapor flux. The power density is defined as the ratio of power and laser beam area.

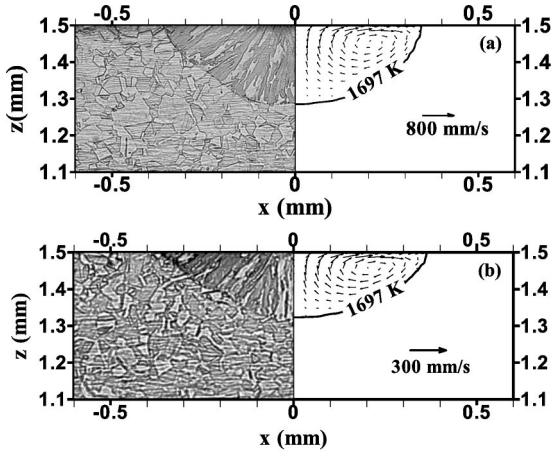

FIG. 6. Experimental and calculated weld pool cross sections. Laser power: 1067 W and pulse duration: 3 ms; (a) beam radius: 0.325 mm and (b) beam radius: 0.466 mm.

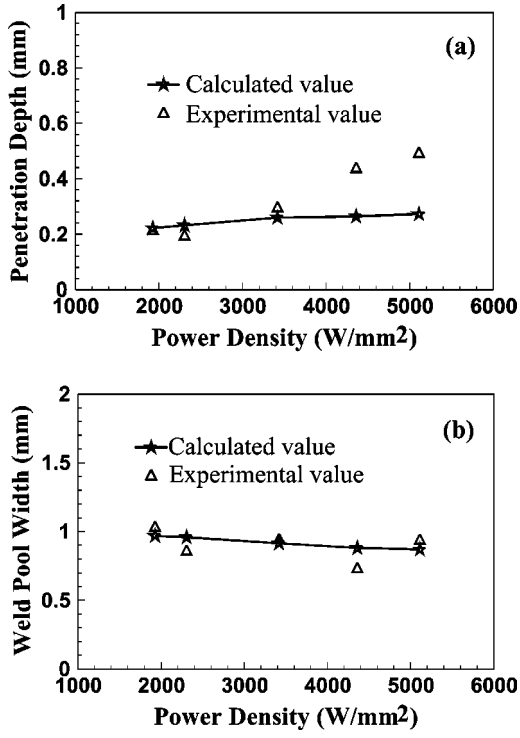

FIG. 7. The effects of laser power density on (a) the weld pool depth, (b) the weld pool width, and (c) the weld pool volume; laser power: 1967 W, and pulse duration: 3.0 ms. The power density is defined as the ratio of power and laser beam area.

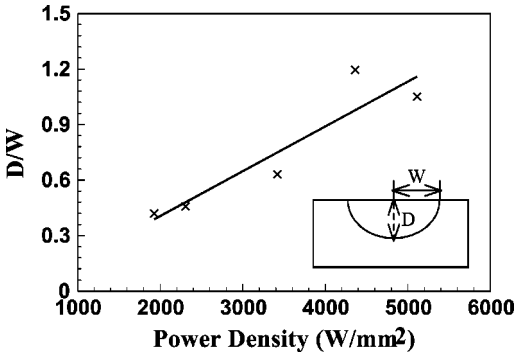

FIG. 8. The variation of D/W with laser power density; laser power: 1967 W and pulse duration: 3.0 ms.

3500 W/mm^2 while this value increased to over 1.0 at higher power densities. Weld pool depths higher than the half-width are often obtained when the surface of the weld pool is significantly depressed from its nearly flat position. Such depressions are common at high power densities, because the high vapor flux exerts significant recoil force on the weld pool surface. In extreme cases, when the recoil force exceeds the surface tension force, fine metal droplets are ejected from the weld pool. Significant loss of mass due to vaporization and metal particle ejection can occur at high power densities.[13] However, the difference between the experimental and the computed values of weld pool depth at power density higher than 3500 W/mm^2 is consistent with the mass loss due to vaporization and particle ejection. At lower power densities, experimentally measured and computed values of weld pool depth and width agree better with the corresponding measured values.

Figures 9(a)–9(e) show the computed temperature and velocity fields as a function of time. The liquid metal motion in the weld pool is driven mainly by the surface tension force and to a much lower extent by the buoyancy force. Because of the negative values of the temperature coefficient of surface tension, the surface tension drives the liquid metal from the center to the periphery at the top surface of the weld pool. As a result, the weld pool becomes wide and shallow. During the initial period of laser spot welding, the weld pool grows rapidly in size and the temperature and velocity of liquid increase with time. At the end of the pulse, the peak temperature and velocity of liquid drops and the weld pool shrinks rapidly. The maximum velocity of liquid in the weld pool is 0.86 m/s. After 5.0 ms, i.e., 1.0 ms after the laser is switched off, the maximum velocity is still about 4.1 mm/s, which is driven mainly by inertia.

A two-phase solid–liquid mushy zone exists in the thin region between the solidus (1697 K) and liquidus (1727 K) temperatures. The size of this zone is very small during heating [as shown in Figs. 9(a)–9(c)]. After the pulse is switched off, the mushy zone begins to expand [shown in Figs. 9(d) and 9(e)], which could be explained by considering the effect of the latent heat of fusion. When the temperature is higher than the liquidus temperature, the heat loss is accompanied by the decrease in temperature. As the temperature drops between the liquidus and solidus temperatures, the heat loss comes mainly from the release of the latent heat of fusion

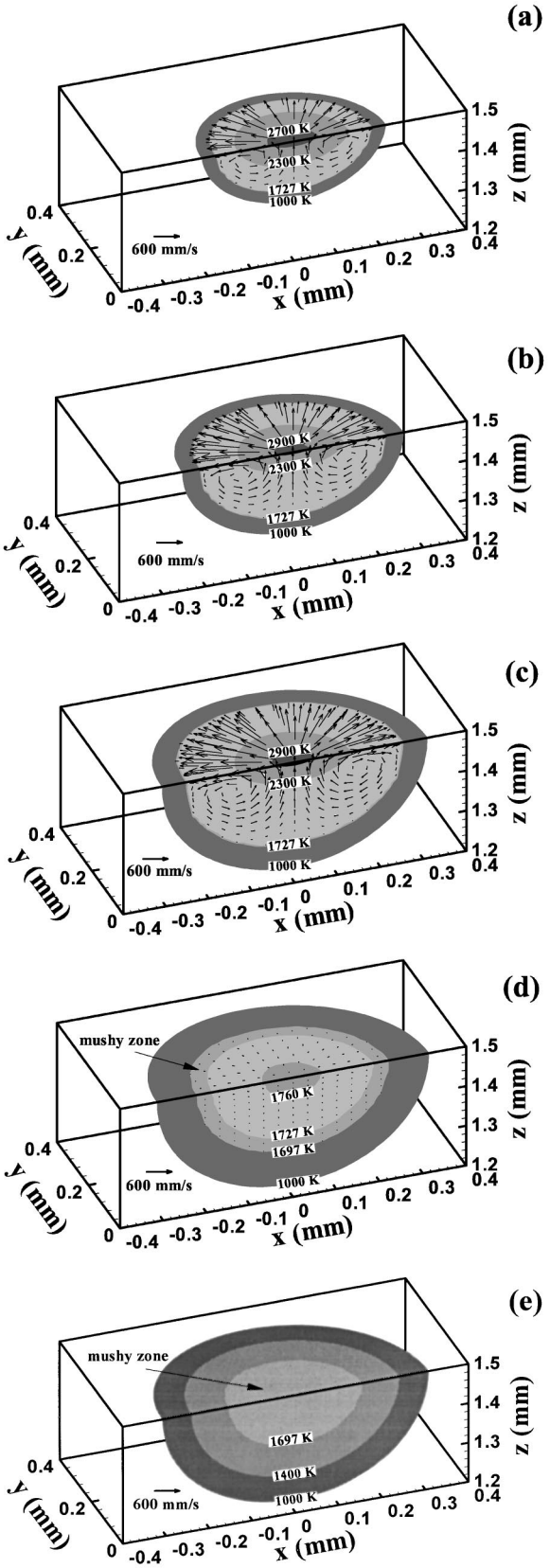

FIG. 9. Computed temperature and velocity fields at different times: (a) $t=1$ ms, (b) $t=2$ ms, (c) $t=4$ ms, (d) $t=4.5$ ms, and (e) $t=5$ ms; laser power: 530 W, pulse duration: 4.0 ms, and spot radius: 0.171 mm.

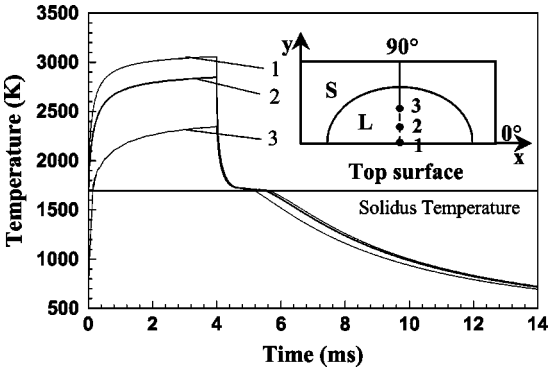

FIG. 10. Weld thermal cycles at different locations on the top surface of weld pool. Distance from the weld center: (1) 0.0 mm; (2) 0.058 mm; (3) 0.125 mm, as shown in the inset. The solid horizontal line indicates solidus temperature; laser power: 530 W, pulse duration: 4.0 ms, and beam radius: 0.171 mm.

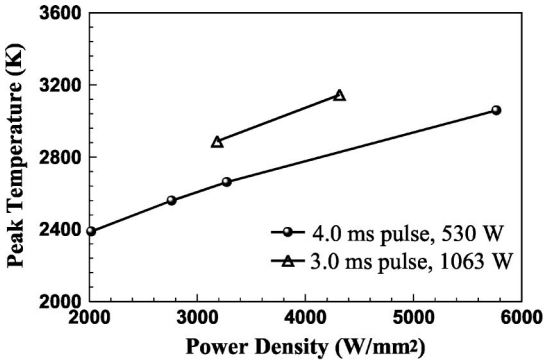

FIG. 11. The variation of peak temperature on the weld pool surface with laser power density.

and the temperature decrease is very slow. The existence of mushy zone has significant effect on the final solidified microstructure.

Figure 10 shows changes in the computed temperatures at three selected locations as a function of time. These locations represent distances of 0, 0.058 and 0.125 mm, respectively, from the location of the heat source, as shown in the small figure. The results indicate that the peak temperatures and the heating rates at different locations vary significantly. The weld pool solidifies completely in about 1.66 ms after the laser pulse is switched off. After the solidification starts, the temperature decreases quickly until it is close to the liquidus temperature. At this temperature, there is a plateau in the thermal cycle curves indicating very low cooling rate due to the release of the latent heat of fusion. Depending on the position, the cooling rates above the liquidus temperature vary significantly. However, as the weld metal cools, the spatial variation of the cooling rates decreases. In the 1073–873 K range, the variation of the cooling rate with temperature is small due to nearly constant outward heat loss from all locations of the weld. Thus, in steels where the final microstructure is determined by the cooling rate through this temperature range, the spatial variation of the microstructure is expected to be small.

The variation of the computed peak temperature with power density is shown in Fig. 11. The peak temperature represents the highest values on the weld pool surface at the end of the pulse. It is also observed from this figure that for the same power energy and same pulse duration, a higher pulse density results in higher peak temperature. The comparison of peak temperature calculated from the numerical heat transfer and fluid flow model with the effective weld pool temperature estimated from the vapor composition is shown in Table III. It can be seen that the temperatures from the model are in fair agreement with the effective temperatures determined from the vapor composition. Thus, the vapor composition can provide a useful estimate of the weld pool peak temperature.

V. SUMMARY AND CONCLUSIONS

Weld pool peak temperature during laser spot welding of 304 stainless steel has been investigated experimentally and theoretically. Experimental work involved determination of composition of the metal vapor by condensing a portion of the vapor on the inner surface of an open ended quartz tube which was mounted perpendicular to the sample surface and coaxial with the laser beam. Iron, chromium and manganese were identified as the main metallic species in the vapor phase. Relative to the alloy composition, the concentrations of Fe and Cr in the vapor increased slightly while the concentration of Mn in the vapor decreased somewhat with the increase in power density. The vapor composition was used to determine an effective temperature of the weld pool. A three-dimensional, transient, numerical model was used to calculate the temperature and velocity fields in the weld pool as a function of time. The experimentally determined geometry of the spot welds agreed well with that determined from the computed temperature field. The effective temperature

TABLE III. Temperatures calculated from vapor compositions and numerical model.

Sample	Power (W)	Radius (mm)	Power density (W/mm^2)	Temperature (K)		
				By transient model	By the value of J_{Fe}/J_{Mn}	By the value of J_{Cr}/J_{Mn}
E	530	0.289	2020	2388	2625	2605
B/F	530	0.247	2765	2559	2800	2775
C	530	0.227	3274	2661	2900	2870
D	530	0.171	5769	3058	3265	3190
G	1063.3	0.326	3185	2888	2885	2855
A	1063.3	0.28	4317	3145	3075	3030

determined from the vapor composition was found to be close to the numerically computed peak temperature at the weld pool surface. Estimation of the approximate values of peak temperature during laser spot welding by measuring vapor composition overcomes the problems encountered in direct measurement of peak temperatures.

ACKNOWLEDGMENTS

The work was supported by a grant from the U.S. Department of Energy, Office of Basic Energy Sciences, Division of Materials Sciences, under Grant No. DE-FGO2-01ER45900. The authors would like to thank Jerome Norris and Paul Hlava for their help with the experimental measurements. Portions of this work were performed at Sandia National Laboratories, which is a multiprogram laboratory operated by Sandia Corporation, a Lockheed Martin Company, for the United States Department of Energy's National Nuclear Security Administration under Contract No. DE-AC04-94AL85000. Valuable critical comments from Dr. C. L. Kim during the preparation of the manuscript are appreciated.

APPENDIX: EQUILIBRIUM VAPOR PRESSURE DATA USED FOR THE CALCULATIONS

The equilibrium vapor pressures of the various vaporizing species over pure liquid were calculated using the following equations.[49–52] In these equations, the vapor pressure is expressed in atm and the temperature is in K

$$\log(P^0_{\mathrm{Fe}}\times 760) = 11.5549 - 1.9538\times 10^4\frac{1}{T} - 0.62549\log T - 2.7182\times 10^{-9}T + 1.9086\times 10^{-13}T^2,$$

$$\log(P^0_{\mathrm{Mn}}\times 1.013\times 10^5) = -5.58\times 10^{-4}T - 1.503\times 10^{-4}\frac{1}{T} + 12.609,$$

$$\log(P^0_{\mathrm{Cr}}\times 1.013\times 10^5) = -13.505\times 10^3\frac{1}{T} + 33.658\log T - 9.29\times 10^{-3}T + 8.381\times 10^{-7}T^2 - 87.077,$$

$$\log P^0_{\mathrm{Ni}} = 6.666 - 20765\frac{1}{T}.$$

Assuming that the solution is ideal at high temperatures, the equilibrium vapor pressures of the various species over the alloy can be expressed as

$$P_i = X_i P_i^0,$$

where X_i is the mole fraction of element i in the alloy and P_i^0 is the equilibrium vapor pressure of element i over the pure liquid.

[1] X. He, P. W. Fuerschbach, and T. DebRoy, J. Phys. D **36**, 1388 (2003).
[2] W. Zhang, G. Roy, J. Elmer, and T. DebRoy, J. Appl. Phys. **93**, 3022 (2003).
[3] A. Block-Bolten and T. W. Eager, Metall. Trans. B **15B**, 461 (1984).
[4] G. J. Dunn, C. D. Allemand, and T. W. Eagar, Metall. Trans. A **17A**, 1863 (1986).
[5] G. J. Dunn and T. W. Eagar, Metall. Trans. A **17A**, 1871 (1986).
[6] A. Blake and J. Mazumder, J. Eng. Ind. **107**, 275 (1985).
[7] D. W. Moon and E. A. Metzbower, Weld. J. (Miami) **62**, 53s (1983).
[8] M. J. Cieslak and P. W. Fuerschbach, Metall. Trans. B **19B**, 319 (1988).
[9] K. Mundra and T. DebRoy, Metall. Trans. B **24B**, 145 (1993).
[10] H. Zhao and T. DebRoy, Metall. Trans. B **32B**, 163 (2001).
[11] P. A. A. Khan and T. DebRoy, Metall. Trans. B **15B**, 641 (1984).
[12] M. M. Collur, A. Paul, and T. DebRoy, Metall. Trans. B **18B**, 733 (1987).
[13] S. Basu and T. DebRoy, J. Appl. Phys. **72**, 3317 (1992).
[14] S. A. David and T. DebRoy, Science **257**, 497 (1992).
[15] T. DebRoy and S. A. David, Rev. Mod. Phys. **67**, 85 (1995).
[16] H. Zhao, D. R. White, and T. DebRoy, Int. Mater. Rev. **44**, 238 (1999).
[17] G. M. Oreper, J. Szekely, and T. W. Eager, Metall. Trans. B **17B**, 735 (1986).
[18] S. Kou and D. K. Sun, Metall. Trans. A **16A**, 203 (1985).
[19] S. Kou and Y. H. Wang, Metall. Trans. A **17A**, 2271 (1986).
[20] M. C. Tsai and S. Kou, Int. J. Numer. Methods Fluids **9**, 1503 (1989).
[21] S. Kou, Weld. J. (Miami) **65**, S63 (1986).
[22] C. Chan, J. Mazumder, and M. M. Chen, Metall. Trans. A **15A**, 2175 (1984).
[23] K. Mundra, T. DebRoy, and K. M. Kelkar, Numer. Heat Transfer **29**, 115 (1996).
[24] W. Pitscheneder, T. DebRoy, K. Mundra, and R. Ebner, Weld. J. (Miami) **75**, 71s (1996).
[25] A. Paul and T. DebRoy, Metall. Trans. B **19B**, 851 (1988).
[26] Z. Yang and T. DebRoy, Sci. Technol. Weld. Joining **2**, 53 (1997).
[27] Z. Yang and T. DebRoy, Metall. Trans. B **30B**, 483 (1999).
[28] W. Zhang, J. W. Elmer, and T. DebRoy, Mater. Sci. Eng., A **333**, 320 (2002).
[29] T. Hong, W. Pitscheneder, and T. DebRoy, Sci. Technol. Weld. Joining **3**, 33 (1998).
[30] T. Hong and T. DebRoy, Metall. Trans. B **34B**, 267 (2003).
[31] T. Hong and T. DebRoy, Ironmaking Steelmaking **28**, 450 (2001).
[32] S. Sista and T. DebRoy, Metall. Trans. B **32B**, 1195 (2001).
[33] Z. Yang, S. Sista, J. W. Elmer, and T. DebRoy, Acta Mater. **48**, 4813 (2000).
[34] S. Sista, Z. Yang, and T. DebRoy, Metall. Trans. B **31B**, 529 (2000).
[35] H. Zhao and T. DebRoy, J. Appl. Phys. **35**, 10089 (2003).
[36] S. V. Patankar, *Numerical Heat Transfer and Fluid Flow* (Hemisphere, New York, 1980).
[37] V. R. Voller and C. Prakash, Int. J. Heat Mass Transfer **30**, 1709 (1987).
[38] A. D. Brent, V. R. Voller, and K. J. Reid, Numer. Heat Transfer **13**, 297 (1988).
[39] C. L. Chan, R. Zehr, J. Mazumder, and M. M. Chen, in *Modeling and Control of Casting and Welding Processes*, edited by S. Kou and R. Mehrabian (TMS, Warrendale, PA, 1986), p. 229.
[40] D. A. Cremers, G. K. Lewis, and D. R. Korzekwa, Weld. J. (Miami, FL, U. S.) **70**, 159s (1991).
[41] J. F. Ready, *LIA Handbook of Laser Materials Processing* (Magnolia, Orlando, 2001).
[42] M. A. Bramson, *Infrared Radiation: A Handbook for Applications* (Plenum, New York, 1968).
[43] D. Peckner and I. M. Bernstein, *Handbook of Stainless Steels* (McGraw–Hill, New York, 1977).
[44] P. W. Fuerschbach and J. T. Norris, Presented at International Conference on Application of Lasers and Electro-optics, Scottsdale, AZ, 14–17 October 2002.
[45] J. R. Davis, *Metals Handbook* (ASM International, Materials Park, OH, 1998).
[46] *ASM Specialty Handbook, Stainless Steel* (ASM International, Materials Park, OH, 1994).
[47] *Metals Handbook*, Volume 1. Properties and Selection: Ion, Steels, and High-Performance Alloys (ASM International, Materials Park, OH, 1990).
[48] F. D. Richardson, *Physical Chemistry of Melts in Metallurgy* (Academic, London, 1974).
[49] R. Hultgren, P. D. Desai, D. T. Hawkins, M. Gleiser, K. K. Kelley, and D.

D. Wagman, *Selected Values of the Thermodynamic Properties of the Elements* (ASM International, Materials Park, OH, 1973).
[50] R. E. Honig and D. A. Kramer, *Physicochemical Measurements in Metal Research* (Interscience, New York, 1970).
[51] C. L. Yaws, *Handbook of Vapor Pressure* (Gulf Publishing Co., Houston, 1994).
[52] C. B. Alcock, V. P. Itkin, and M. K. Horrigan, Can. Metall. Q. **23**, 309 (1984).